

Direct Numerical Simulation of Shock-Induced Drop Breakup with a Sharp-Interface-Method

Jakob W. J. Kaiser*, Stefan Adami¹, Nikolaus A. Adams²

Technical University of Munich
Department of Mechanical Engineering
Chair of Aerodynamics and Fluid Mechanics
Boltzmannstraße 15, 85748 Garching, Germany
*jakob.kaiser@tum.de

ABSTRACT

We present two- and three-dimensional numerical results of the shock-induced breakup of a liquid droplet in air. We apply a conservative interface interaction model for sharp-interface representation and a block-based multi-resolution scheme to adaptively refine our mesh. Numerical modeling effects, such as the flux reconstruction scheme and the use of a scale separation model, that treats non-resolved interface segments, are investigated. Similarly as a previous study (Meng, 2016), we identify two dominant mechanisms of droplet breakup at certain Mach numbers - flattening of the droplet and sheet stripping - occurring simultaneously and influencing each other in our simulations. Three-dimensional simulations show the flattening mechanism and the mushroom-like deformation of the droplet. They also explain the occurrence of a recirculation zone in the droplet wake. The two-dimensional simulations already exhibit the sheet stripping mechanism, which occurs during and after droplet flattening. Small sheets emerge from both the upstream and the downstream side of the 2D droplet, while the main sheet develops at the droplet equator.

INTRODUCTION

Droplet breakup, i.e. the breakup of an initially spherical drop into smaller fragments due to the velocity difference to the ambient flow field, is relevant to a wide range of technical systems, e.g. the breakup of liquid jets in combustion engines. An extensive review on gas-liquid secondary atomization has been lately published by Guildenbecher *et al.* (2009), underlining that there is no direct link between increasing velocity differences and smaller drop sizes. To control the final droplet size, hence, a detailed knowledge of the underlying physics is necessary. Due to the inherent difficulties of analyzing droplet breakup experimentally - especially due to small local and temporal scales (Theofanous, 2011) - and increasing computational capabilities, direct numerical simulation emerges as possible choice for detailed investigations.

Many studies so far have been limited to two dimensions (2D) (Igra & Takayama, 2001) or assume cylindrical symmetry (Aalburg *et al.*, 2003; Han & Tryggvason, 2001). Among the first to perform fully three-dimensional (3D) simulations of droplet fragmentation were Khosla *et al.* (2006), who used the VOF method to investigate the transition between different breakup mechanisms in a lower Weber number range. According to Guildenbecher *et al.* (2009), 2D and 3D simulations of droplet breakup yield physically similar results. Recently, Meng (2016) investigated the early stages of droplet breakup with a highly resolved fully 3D simulation of a water drop in air exposed to a shock with Mach number $M_S = 1.47$. She used a non-adaptive cylindrical grid and the volume-of-fluid (VOF) approach to capture the interface.

In this work, we investigate droplet breakup dynamics with a conservative interface interaction method for sharp-interface representation and low-dissipation nonlinear discretization schemes on an adaptive mesh, applying a block-based multi-resolution algorithm. 2D and 3D simulations of a water droplet in air flow are conducted for a shock Mach number of $M_S = 1.47$. We employ a block-based multi-resolution code with sharp-interface capturing (level-set) and high resolution shock capturing. We investigate the effect of removing under-resolved interface structures using a scale-separation technique (Luo *et al.*, 2016) and show differences between the more dissipative WENO-5 and the less dissipative WENO-CU6. We compare the results of our sharp-interface (level-set) approach with the diffuse-interface method (VOF) of Meng.

NUMERICAL MODEL

Governing Equations And Discretization

The compressible Euler equations including surface tension

$$\frac{\partial \mathbf{U}}{\partial t} + \nabla \cdot \mathbf{F}(\mathbf{U}) = \mathbf{S} \quad (1)$$

with

$$\mathbf{U} = \begin{pmatrix} \rho \\ \rho \mathbf{u} \\ E \end{pmatrix} \quad \mathbf{F}(\mathbf{U}) = \begin{pmatrix} \mathbf{u}\rho \\ \rho \mathbf{u} \otimes \mathbf{u} + p\mathbf{I} \\ \mathbf{u}(E+p) \end{pmatrix} \quad \mathbf{S} = \nabla \cdot \begin{pmatrix} 0 \\ \kappa \sigma \mathbf{N} \\ \kappa \sigma \mathbf{N} \cdot \mathbf{u} \end{pmatrix} \quad (2)$$

are solved, closed by applying the stiffened gas EOS

$$p = (\gamma - 1)\rho e - \gamma \Pi. \quad (3)$$

Here, ρ is the density, \mathbf{u} the velocity vector, E the total energy, p the pressure, \mathbf{I} the identity matrix, κ the local interface curvature, σ the surface tension coefficient, \mathbf{N} the local normal vector on the interface, γ the ratio of specific heats, e the internal energy, and Π the reference pressure for the stiffened gas EOS.

We apply a finite-volume discretization scheme on cubic cells with characteristic flux projection for the hyperbolic part (Roe, 1981) and global Lax-Friedrichs (GLF) flux splitting. For flux reconstruction at the cell faces from cell averages, the 5th-order WENO scheme (Jiang & Shu, 1996) or the central-upwind 6th-order WENO scheme (Hu & Adams, 2011) are used. The basic idea of WENO schemes is to apply low-dissipative, high order stencils in smooth flow regions, while falling back to non-linear convex combinations of lower-order stencils in regions with large gradients.

¹stefan.adami@tum.de

²nikolaus.adams@tum.de

The WENO-CU6 scheme, furthermore, adapts between central and upwind schemes, providing sixth-order accuracy in smooth regions, good shock-capturing properties and low numerical dissipation. For the interface interaction including surface tension, an acoustic Riemann solver is applied (Saurel *et al.*, 2003). For time discretization, the 2nd-order Runge-Kutta TVD time integration scheme of Gottlieb & Shu (1998) is used. The timestep size is limited by the CFL-condition

$$\Delta t \leq \text{CFL} \frac{1}{\sum_i \frac{|u_i + c|}{\Delta x_i}} \quad (4)$$

with the speed of sound c , the cell width in i -direction Δx_i , $i \in \{1, 2\}$ for two-dimensional and $i \in \{1, 2, 3\}$ for three-dimensional simulations. The CFL-number is set to $\text{CFL} = 0.6$.

Sharp-Interface Method

For interface capturing, a level-set function, ϕ , is employed. It describes the signed distance from the cell center to the interface, with the zero-level-set representing the interface and $|\nabla\phi| = 1$. The level-set field is propagated by solving the advection equation

$$\frac{\partial\phi}{\partial t} + \mathbf{u}_\phi \cdot \nabla\phi = 0 \quad (5)$$

with \mathbf{u}_ϕ being the evolution velocity of the level-set. To maintain the constraint $|\nabla\phi| = 1$, the level-set field is re-initialized at every time instant applying the one-step reinitialization of Fu *et al.* (2015).

Evolving the interface may generate structures which cannot be well resolved on the given mesh. These structures may introduce spurious fluctuations, which eventually may lead to numerical instabilities (Hu & Adams, 2011). To identify non-resolved structures and reconstruct a well resolved interface, the scale separation method of Luo *et al.* (2016) is applied. It uses additional auxiliary level-sets ε which employ the local mesh size to separate non-resolved from resolved interface segments and apply a re-distancing function to compute the reconstructed level-set field.

Multi Resolution

The block-based multi-resolution method developed by Han *et al.* (2014) is used for achieving efficient high-resolution simulations. It employs a pyramid based data-structure where cell-averaged data (\bar{U}) on level l can be computed from level $l+1$ using the projection operator

$$P_{l+1 \rightarrow l} : \bar{U}_{l+1} \rightarrow \bar{U}_l \quad (6)$$

and cell-averaged data on level $l+1$ can be estimated from level l using the prediction operator

$$P_{l \rightarrow l+1} : \bar{U}_l \rightarrow \hat{U}_{l+1}. \quad (7)$$

The differences between predicted and cell-averaged data, the so-called details

$$\bar{d}_{l,i} = \bar{U}_{l,i} - \hat{U}_{l,i} \quad (8)$$

are then used to determine the required resolution in space to achieve a given accuracy (Harten, 1996). The decision whether a

block needs to be refined or may be coarsened is made by comparing the details to a level dependent threshold. E.g., when droplets move further downstream, the mesh is refined locally, while regions further upstream are coarsened. This allows for investigating also later stages of droplet breakup efficiently.

Droplet Diagnostics

Besides qualitative breakup analysis based on the interface deformation, we conduct quantitative investigations considering the interface deformation and the variation of center-of-mass related properties for our two-dimensional simulations. The quantities and, if necessary, their corresponding definitions are chosen as proposed by Meng (2016). The analyzed quantities are:

- the deformed droplet diameter, D_d , which is the elongated drop width (y-direction),
- the streamwise drift of the upstream stagnation point, Δx_{sp} ,
- the streamwise drift of the center of mass for the liquid phase Ω

$$x_c = \frac{\int_{\Omega} \rho_l x dV}{\int_{\Omega} \rho_l dV}, \quad (9)$$

where ρ_l denotes the cell-averaged density of the liquid phase and x the streamwise cell center coordinate, and

- the streamwise center-of-mass acceleration

$$a_c = \frac{d^2 x_c}{dt^2} = \frac{\int_{\Omega} \frac{\partial}{\partial t} (\rho_l u) dV}{\int_{\Omega} \rho_l dV}, \quad (10)$$

where u denotes the cell-averaged streamwise velocity component.

Non-dimensionalization

Note that all results are non-dimensionalized. Length scales are non-dimensionalized with the initial drop diameter D_0 , velocity scales with the post-shock velocity u_s , the acceleration with u_s^2/D_0 , and time-scales by

$$t_{ref} = \frac{D_0}{u_s} \sqrt{\frac{\rho_l}{\rho_s}}. \quad (11)$$

ρ_s denotes the density of post shock air (Meng, 2016). Non-dimensional parameters are marked by an asterisk (*).

TWO-DIMENSIONAL INVISCID SIMULATION Setup

We use 2D inviscid simulations to investigate the influence of numerical parameters and mesh refinement, and to analyze the results in detail. Simulations are performed at shock Mach number $M_S = 1.47$ in standard air ($\gamma = 1.4$, $\Pi = 0 \text{ N/m}^2$) and with a water column ($\gamma = 6.12$, $\Pi = 3.43 \times 10^8 \text{ N/m}^2$) of initial diameter $D_0 = 4.8 \text{ mm}$. Post-shock parameters are $\rho_s/\rho_0 = 1.811$, $u_s/c_s = 0.5755$, and $p_s/p_0 = 2.354$. The surface tension coefficient for water and air is $\sigma = 72.75 \times 10^{-3} \text{ N/m}$. A section of the simulated domain is shown in Figure 1. Both the initialization (upper half) and the grid at $t^* = 0.025$ (lower half) are displayed to demonstrate the grid adaptivity with the evolving flow field. Assuming axial symmetry, we only simulate one half of the domain. At the centerline, we choose a symmetry boundary condition, all other boundaries are outflow boundary conditions. We perform all our simulations to a final time of $t^* = 1.5$.

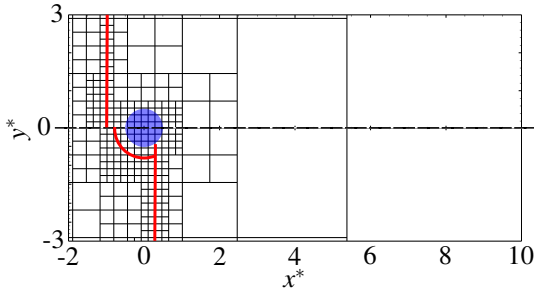


Figure 1. Simulation domain with grid at a resolution of 1:16 and most important flow field features sketched. The upper half shows the grid at initialization, the lower half at $t^* = 0.025$. The droplet is sketched for both instants in blue, the shock in red.

Influence Of Numerical Parameters

For the analysis of the influence of numerical parameters, we consider five different cases:

- Case 1: $\Delta x^* = 0.01$, WENO5, scale separation model.
- Case 2: $\Delta x^* = 0.02$, WENO5, scale separation model.
- Case 3: $\Delta x^* = 0.005$, WENO5, scale separation model.
- Case 4: $\Delta x^* = 0.01$, WENO5, no scale separation model.
- Case 5: $\Delta x^* = 0.01$, WENO-CU6, scale separation model.

Case 1 is our baseline case. We compare all other simulations against its results to estimate the influences of mesh refinement, the scale separation, and the flux reconstruction scheme.

For a first qualitative assessment, we compare the interface morphology and the flow field around the 2D droplet for all cases at $t^* = 1$. Numerical schlieren (upper half) and the normalized velocity field (lower half) are given in Figure 2. The flow direction is from left to right. The droplet interface is marked by a blue line. Focusing first on the 2D droplet morphology in comparison to our baseline case (a), the thin sheet is shorter and thicker for $\Delta x^* = 0.02$ (b). For $\Delta x^* = 0.005$ (c), shape and movement of the sheet are more distinct: it is thinner and strongly curved compared to the baseline case. Furthermore, an additional smaller sheet appears upstream of this main sheet. Drift and shape of the bulk droplet are similar for all three cell sizes, though details of the interface curvature vary. Omitting the scale separation model (d) leads to a longer, thinner sheet, and to small, under-resolved structures (compare to Figure a). The position of the sheet and drift and shape of the bulk droplet are essentially unaffected. However, this simulation becomes under-resolved for $t^* = 1.3$. With the WENO-CU6 scheme (e), the cusp on the downstream side of the droplet is slightly smoothed compared to the baseline case. The drop drift remains basically the same. It also leads to a slightly earlier breakup of the main sheet, even though its size is approximately the same as for the baseline case. The flow field close to the 2D droplet for all five cases can be separated into two main regions: the ambient flow field which is disturbed by the 2D droplet, and the backflow region forming an upstream jet which is generated by unsteady vortex shedding (Meng, 2016). The backflow region will be discussed in the result sections. These two regions can be observed for all cases, independently of the numerical scheme or grid refinement. Compared to the baseline case (a), the coarser mesh (b) results in a more homogeneous backflow region, forming only a narrow shock close to the 2D droplet and no vortices. For the finer mesh (c), the structure of the recirculation zone becomes more complex: the upstream jet moves further downstream, and the shock forms further downstream, too. Closer to the 2D droplet, a complex pattern of multiple recirculation zones appears. Furthermore, an additional recirculation zone arises at the droplet equator near the sheets. With the WENO-CU6

scheme (e), an additional recirculation zone can be observed next to the upstream jet (compared to Figure a). For this scheme, wave dynamics downstream of the droplet are resolved more accurately, leading to finer wave structures and additional vortex generation. The shock in the recirculation zone develops further downstream than for the baseline case.

Next, we analyze integral quantities. Non-dimensionalized quantities for all simulation setups and reference data from Meng (2016) for $M_S = 1.47$ are shown in Figure 3. The drift of the 2D droplet is given in (a), both for the upstream stagnation point (dashed lines) and the center of mass (solid lines). The shift of the upstream stagnation point is mostly independent of the numerical schemes and agrees well with literature results. For the center-of-mass drift, the results are independent of the numerical scheme at early times, too. They differ once the sheet breakup starts for $t^* > 1$, but the general trend is the same. For increasing resolution, the results converge against literature results, with good agreement already for $\Delta x^* = 0.01$. The influence on the deformed droplet diameter (b) is larger: while only case 2 remains within the bounds of the VOF simulation, all other cases develop several peaks. The peaks occur at the same time when the tip of the main sheet breaks up. This sheet is neither fully captured in the 2D simulations of Meng nor by our level-set approach on the coarse mesh. The breakup of the sheet is very sensitive to grid resolution and, to a lesser amount, to numerical dissipation: for $\Delta x^* = 0.01$, the first breakup occurs at $0.98 < t^* < 1.07$, but for $\Delta x^* = 0.005$ at $t^* = 0.70$. After the breakup, D_d is still dominated by the sheet movement and differs to literature results. The sheet growth also influences the center-of-mass acceleration (c). The initial acceleration of the 2D droplet after the shock has passed is similar for all cases and shows good agreement with the VOF simulations. The subsequent acceleration for $0.05 < t^* < 0.3$ is lower in our level-set approach, but shows little variation for the different cases. For $t^* > 0.3$, the acceleration depends on the growth of the sheet and, therefore, differs for cases with different resolution and the VOF results. An acceleration peak can be observed prior to the first drop-off in D_d^* for our cases 1 and 3 to 5. The acceleration then falls off sharply before increasing again.

In summary, our numerical study shows that for all five cases the general behavior of the 2D droplet and the flow field are similar. Quantitative differences occur for the size of the recirculation zone, its separation in a supersonic and a subsonic part, and the number and growth of sheets at the droplet interface.

Results

Now, we consider the setup of case 3 to investigate the unsteady evolution of the breakup. We choose this case as it provides the most detailed insight due to its fine resolution, especially at the sheet stripping mechanism. A visualization of the vicinity of the 2D droplet at several instants is provided in Figure 4 to describe the most important physical aspects of the breakup mechanism as observed in our simulation results. The static pressure field p^* is shown in the upper half, the streamwise velocity field u^* in the lower half. The flow direction is from left to right.

The immediate effect of the shock on the droplet deformation is negligible. The shock has passed the 2D droplet at $t^* = 0.03$, when the droplet still has its initial shape (Figure 3 b). Yet, the reflection of the shock creates a high pressure region at the upstream stagnation point, as well as a bow shock propagating in reverse main flow direction. After the shock traversed over the droplet, the convergence of the Mach stems generates a secondary wave which leads to another pressure increase at the downstream stagnation point, but a minimum close to the equator ($t^* = 0.07$). This non-uniform pressure distribution leads to the flattening of the droplet, which is visible later at $t^* = 0.18$. At the same instant, a small tip can be ob-

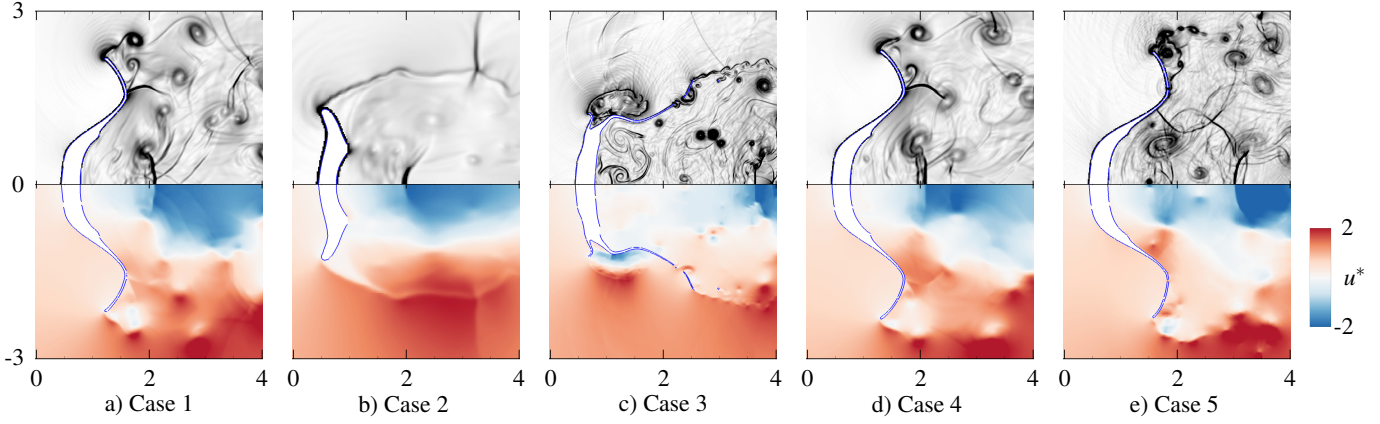


Figure 2. Numerical schlieren image (upper half) and normalized velocity field (lower half) of the flow field in the vicinity of the 2D droplet at $t^* = 1$ for all five setups. The interface is denoted by the blue line.

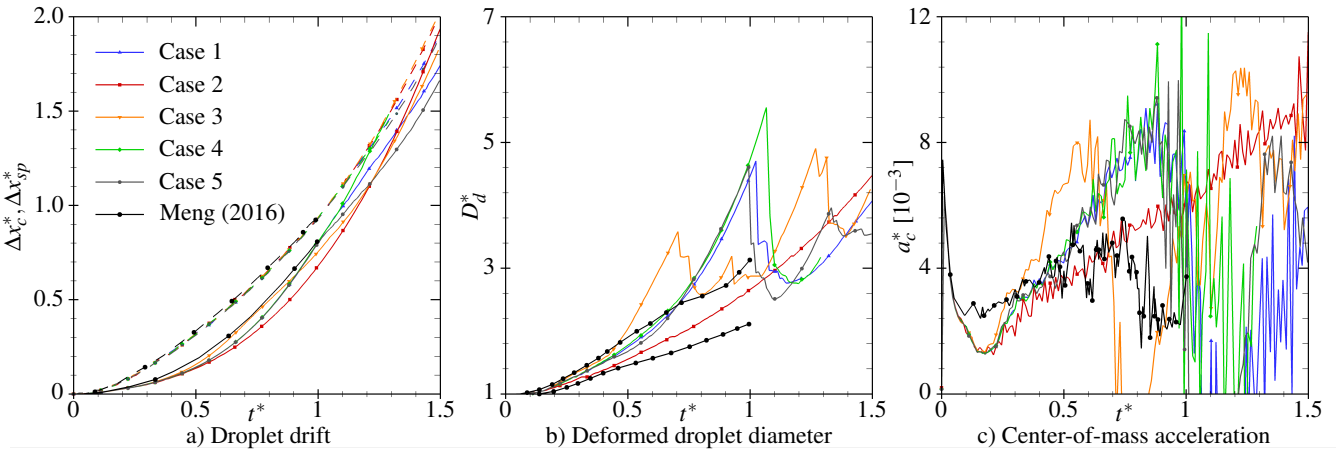


Figure 3. Integral parameters for the five tested cases and comparison data of Meng (2016): stagnation point drift Δx_{sp}^* (dashed) and center-of-mass drift Δx_c^* (solid) (a), deformed droplet diameter D_d^* (b), and center-of-mass acceleration (c). All parameters are given as function of the non-dimensional time t^* and normalized as described above. In b), the upper reference line of Meng denotes a volume fraction of $\alpha = 0.25$, the lower line of $\alpha = 0.99$.

served at the edge of the flattened droplet. It appears where the secondary wave interacts with the droplet interface and is probably caused by local pressure fluctuations. This is the first indicator of the sheet stripping mechanism (Chen, 2008). The cusp grows over time to a single large sheet, whose tip breaks up further downstream, as seen for $t^* > 0.55$. Parts of this sheet are also removed by the scale separation algorithm in case they become too small and are under-resolved. Initially, the sheet breakup is limited to its tip, before larger parts disintegrate for $t^* > 1.23$. The growth and breakup of this sheet is related to fluctuations in the center-of-mass acceleration (see Figure 3 c): the acceleration increases, except for a sharp drop-off around the breakup times (e.g., $t^* = 0.70$). Additional smaller tips are generated by local pressure differences. In our simulation, we see one distinct tip at the upstream and one at the downstream side of the droplet at $t^* = 0.55$. They evolve to small thin sheets, but merge with the large sheet before they are thin enough to break up themselves or are removed as being under-resolved. The origin of these tips is twofold: the downstream tip emerges from the planar downstream droplet segment. The upstream tip emerges from small interface disturbances. It is observed the first time when the secondary wave crosses the droplet equator and detaches from the droplet interface.

The advancing deformation of the 2D droplet leads to unsteady vortex shedding which results in an unsteady recirculation zone in the wake of the droplet. This zone was already described by Meng (2016) for both 2D and 3D simulations. The origin of this recirculation zone is explained later in more detail for the 3D simulation. In our 2D simulations, the recirculation zone is initially supersonic. Later, the deflection of the flow close to the droplet forms a shock with a subsonic region. Additionally to this wake recirculation zone, multiple smaller recirculation zones can be observed at the droplet interface which emerge at the thin liquid sheets. For $t^* = 0.18$, close to the equator of the drop at the emerging tip, a recirculation zone can be observed. This equatorial recirculation zone was found by Meng (2016) to affect the sheet stripping mechanism. This zone is advected together with the emerging sheet and later disappears ($t^* = 0.73$). When the smaller tips are formed up- and downstream of this main sheet, small recirculation zones can be observed there, too. They disappear once the attached sheets merge with the main sheet. An additional, large recirculation zone appears at the tip of the main sheet shortly before it breaks up ($t^* = 1.05$). We believe that it originates from the oscillations of the sheet: when the sheet moves towards the centerline, the previously aligned flow detaches and forms the recirculation zone.

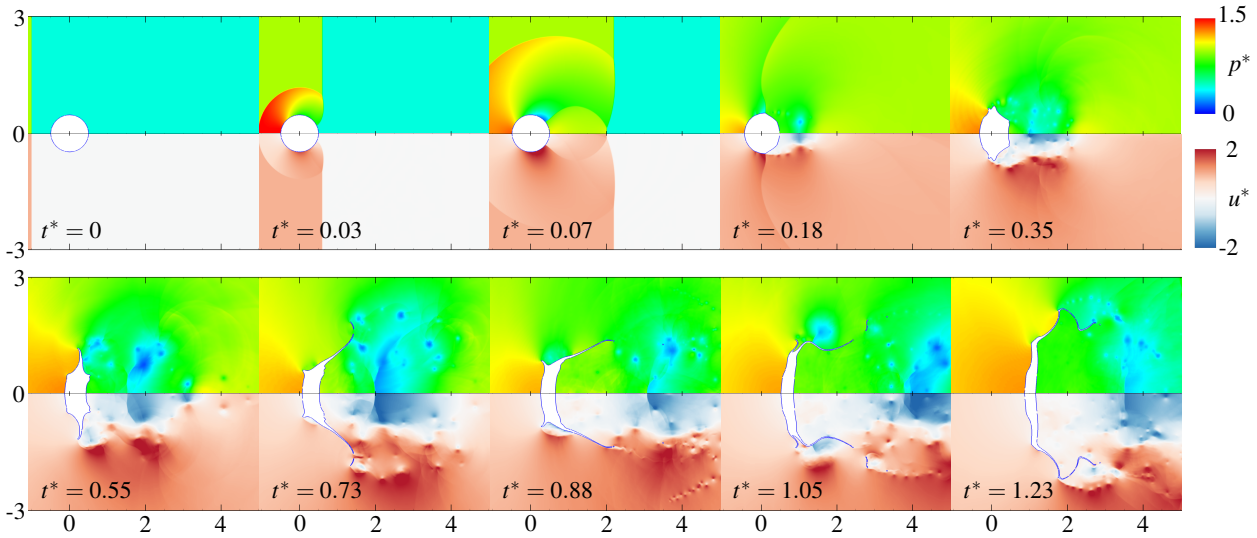


Figure 4. Normalized pressure p^* (upper half) and normalized streamwise velocity component u^* (lower half) at different instants. The interface is marked by the blue line.

THREE-DIMENSIONAL INVISCID SIMULATION

Setup

In the following section, we analyze three-dimensional simulation results. Due to available computer resources available, we are currently limited to a resolution of $\Delta x/D_0 = 0.024$. A full droplet is simulated as shown in Figure 1, with outflow boundary conditions applied at the edge of the domain. The shock Mach number is $M_S = 1.47$, hence the initial conditions are identical to the previous section.

Results

The 3D interface evolution is shown in Figure 5. Note that the time instants are similar to the 2D case in Figure 4. The flow direction is from top right to bottom left, as we focus in our analysis on the interface evolution on the downstream side. The black lines denote x^* -isolines with $\Delta x^* = 0.025$. While during the shock passage the droplet shape does not change, a first flattening can be observed at $t^* = 0.19$ due to the pressure gradient between the upstream and the downstream side of the droplet. This deformation increases and leads to a cave on the downstream side, which first appears at $t^* = 0.66$ and grows further over time, leading to a mushroom-like shape. This interface pattern was already observed by Meng (2016). The absence of thin sheets is due to the coarse resolution of this simulation.

For analyzing the flow field, streamwise velocity and vorticity fields at $t^* = 0.38$ around the droplet are displayed in Figure 6 on the center slice $y^* = 0$. They show both the wake and the equatorial recirculation zone. The vorticity field gives more details on the origin of these two recirculation zones: the flow over the droplet leads to a negative azimuthal vorticity stream from the droplet equator. This generates the upstream jet impinging on the rear part of the droplet and leading to the cave visible in Figure 5 for $t^* > 0.66$. At the back of the droplet close to the downstream stagnation point, the jet is deflected. This generates a positive vorticity stream, which travels towards the droplet equator where it interacts with the negative vorticity stream. This interaction, which was also already observed in the VOF simulations of Meng (2016), then leads to the generation of the equatorial recirculation zone, which is visible in both our 2D and 3D simulations.

CONCLUSION

We have assessed 2D and 3D simulations of aerobreakup with a sharp-interface method (level-set), using a multi-resolution approach to adaptively refine our mesh and coupled with a local time-stepping algorithm. We have assessed the effect of different numerical methods and mesh refinement on our 2D simulation results. We have analyzed the drop deformation and the surrounding flow field for 2D and 3D simulations.

Very good agreement is found compared to the volume-of-fluid approach of Meng (2016). Our approach reproduces the same flow field patterns, especially the recirculation zone downstream of the droplet and its origin in the negative azimuthal vorticity streams. Liu & Reitz (1997) proposed two consecutive major stages of aerobreakup: flattening of the droplet due to the pressure gradient over the droplet and subsequently, for this breakup mode, stripping of thin liquid sheets which disintegrate downstream. As already seen in Meng (2016), our simulation results show that these two mechanisms are closely interconnected, too. The flattening of the droplet can be observed first, caused by the pressure gradient up- and downstream of the droplet. This flattening is followed by the shear stripping mechanism. Meng found in her three-dimensional simulations two sheets: a large sheet emerging from the droplet equator and a smaller one from the planar downstream droplet segment. Our two-dimensional simulations show these two sheets, too. An additional smaller sheet forms at the upstream side of the droplet. We assume that this sheet emerging in the early phase of the breakup is caused by pressure disturbances. They occur at approximately the same time when the secondary shock wave detaches from the droplet.

It remains to determine whether these findings also apply for a 3D setup. Therefore, we currently pursue a distributed-memory version of our code to run fully three-dimensional simulations at the same resolution as our two-dimensional cases.

ACKNOWLEDGMENT

The lead author is supported by the German Research Foundation (Deutsche Forschungsgesellschaft, DFG). The second and third authors acknowledge funding by the European Research Council (ERC) under the European Union's Horizon 2020 research and innovation program (grand agreement No. 667483) The authors gratefully acknowledge the Gauss Centre for Supercomputing e.V. (www.gauss-centre.eu) for funding this project by providing com-

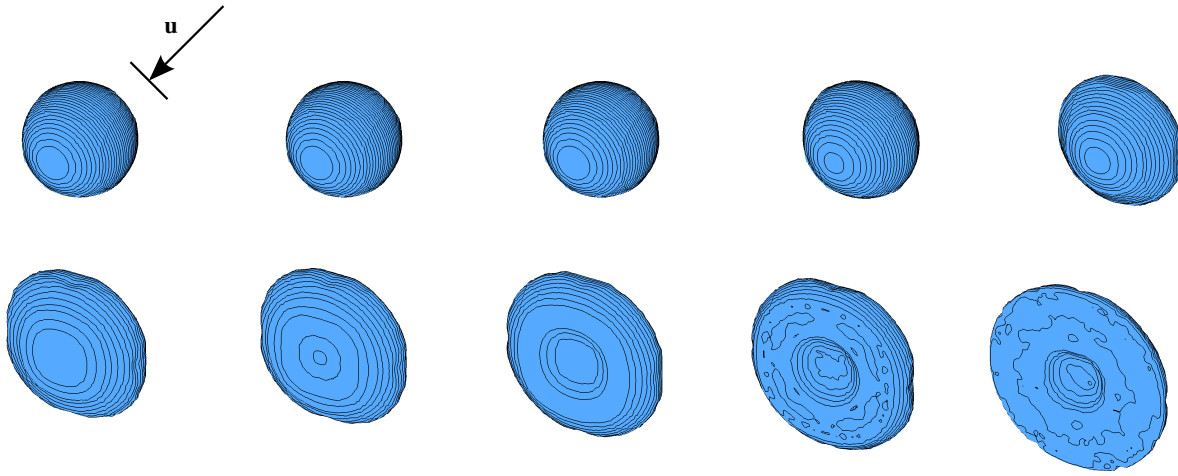


Figure 5. Droplet interface at instants $t^* = \{0, 0.04, 0.06, 0.19, 0.35, 0.56, 0.66, 0.88, 1.06, 1.24\}$ (left to right, top to bottom). Flow direction is from top right to bottom left, as marked by the black arrow. The black lines mark isolines for the axial coordinate with a spacing of $\Delta x^* = 0.025$.

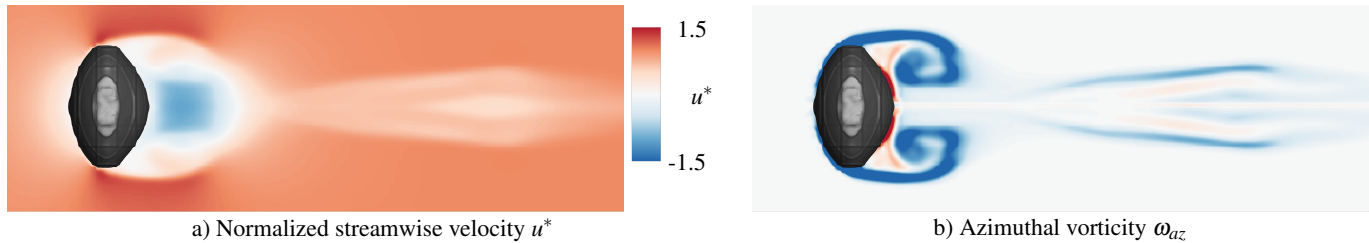


Figure 6. The flow field around the deformed droplet at $t^* = 0.38$ on slice $y^* = 0$. Given are the normalized velocity (a) and the azimuthal vorticity (b), with red marking a positive and blue a negative vorticity. Marked gray is the isosurface $\phi = 0$, i.e. the droplet interface.

puting time on the GCS Supercomputer SuperMUC at Leibniz Supercomputing Centre (www.lrz.de).

REFERENCES

- Aalburg, C., van Leer, B. & Faeth, G. M. 2003 Deformation and Drag Properties of Round Drops Subjected to Shock Wave Disturbances. *AIAA Journal* **41** (12), 2371–2378.
- Chen, H. 2008 Two-dimensional simulation of stripping breakup of a water droplet. *AIAA Journal* **46** (5), 1135–1143.
- Fu, L., Hu, X. Y. & Adams, N. A. 2015 Explicit reinitialization and extending algorithms for level-set based sharp-interface method. In *The ninth Symposium on Turbulence and Shear Flow Phenomena*. Melbourne, Australia.
- Gottlieb, S. & Shu, C.-W. 1998 Total variation diminishing Runge-Kutta schemes. *Mathematics of Computation* **67** (221), 73–85.
- Guildenbecher, D. R., López-Rivera, C. & Sojka, P. E. 2009 Secondary atomization. *Experiments in Fluids* **46** (3), 371–402.
- Han, J. & Tryggvason, G. 2001 Secondary breakup of axisymmetric liquid drops. II. Impulsive acceleration. *Physics of Fluids* **13** (6), 1554–1565.
- Han, L. H., Hu, X. Y. & Adams, N. A. 2014 Adaptive multi-resolution method for compressible multi-phase flows with sharp interface model and pyramid data structure. *Journal of Computational Physics* **262**, 131–152.
- Harten, A. 1996 Multiresolution Algorithms for the Numerical Solution of Hyperbolic Conservation Laws. *Communications on Pure and Applied Mathematics* **48**, 1305–1342.
- Hu, X.Y. & Adams, N.A. 2011 Scale separation for implicit large eddy simulation. *Journal of Computational Physics* **230** (19), 7240–7249.
- Igra, D. & Takayama, K. 2001 Numerical simulation of shock wave interaction with a water column. *Shock Waves* **11** (3), 219–228.
- Jiang, G.-S. & Shu, C.-W. 1996 Efficient Implementation of Weighted ENO Schemes. *Journal of Computational Physics* **126**, 202–228.
- Khosla, S., Smith, C. E. & Throckmorton, R. P. 2006 Detailed Understanding of Drop Atomization by Gas Crossflow Using the Volume of Fluid Method. In *19th Annual Conference on Liquid Atomization and Spray Systems (ILASS Americas)*. Toronto, Canada.
- Liu, Z. & Reitz, R. D. 1997 An analysis of the distortion and breakup mechanisms of high speed liquid drops. *International Journal of Multiphase Flow* **23** (4), 631–650.
- Luo, J., Hu, X. Y. & Adams, N. A. 2016 Efficient formulation of scale separation for multi-scale modeling of interfacial flows. *Journal of Computational Physics* **308**, 411–420.
- Meng, J. C. 2016 Numerical Simulations of Droplet Aerobreakup. PhD thesis, California Institute of Technology, Pasadena, CA.
- Roe, P. L. 1981 Approximate Riemann Solvers, Parameter Vectors, and Difference Schemes. *Journal of Computational Physics* **43**, 357–372.
- Saurel, R., Gavriluk, S. & Renaud, F. 2003 A multiphase model with internal degrees of freedom: application to shockbubble interaction. *Journal of Fluid Mechanics* **495**, 283–321.
- Theofanous, T. G. 2011 Aerobreakup of Newtonian and Viscoelastic Liquids. *Annual Review of Fluid Mechanics* **43** (1), 661–690.